# AIAA 2004–1231

# CFD Visualization of Second Primary Vortex Structure on a 65-Degree Delta Wing

**Kazuhisa Chiba, Shigeru Obayashi**
*Institute of Fluid Science, Tohoku University, Sendai, Japan*

**and Kazuhiro Nakahashi**
*Department of Aeronautics and Space Engineering, Tohoku University, Sendai, Japan*

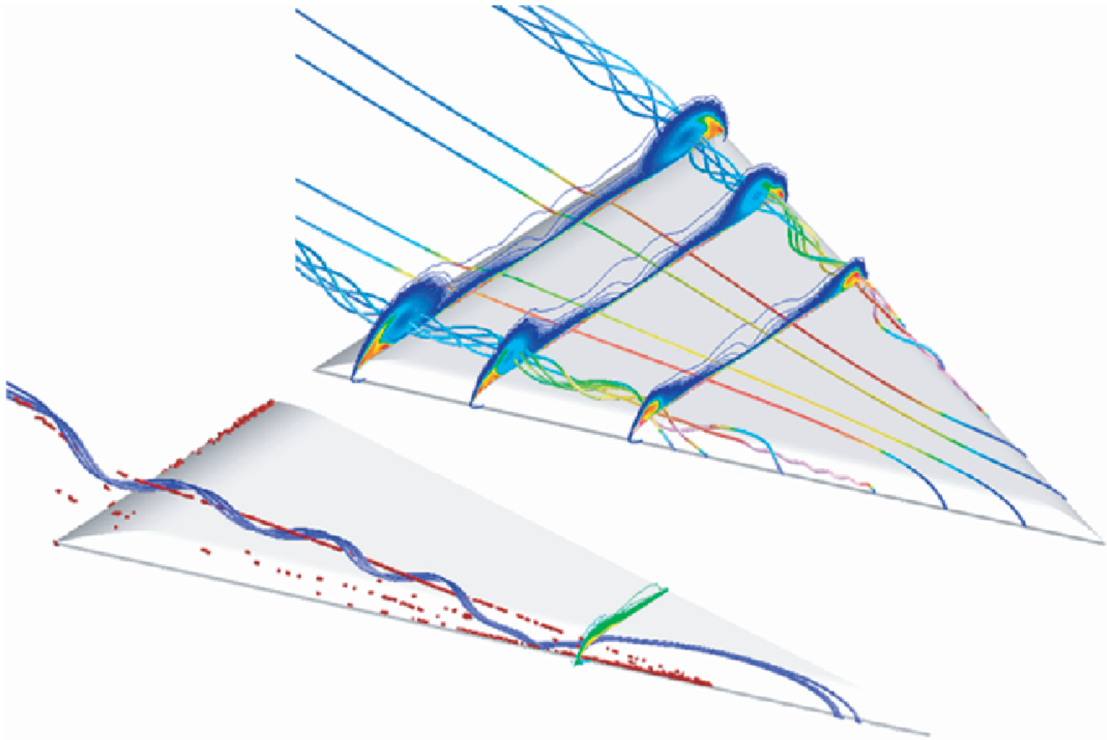

**42nd AIAA Aerospace Sciences Meeting and Exhibit**
**January 5–8, 2004/Reno, NV**

# CFD Visualization of Second Primary Vortex Structure on a 65-Degree Delta Wing

Kazuhisa Chiba,* Shigeru Obayashi†
*Institute of Fluid Science, Tohoku University, Sendai, Japan*
and Kazuhiro Nakahashi‡
*Department of Aeronautics and Space Engineering, Tohoku University, Sendai, Japan*

## Abstract

Numerical simulation has been performed corresponding to recent experiment around delta wings with sharp and blunt leading edges at NASA Langrey Research Center, which indicates the second primary vortex and quantitative Reynolds-number effects. Three one-equation turbulence models are examined on the unstructured hybrid mesh and the modified Spalart-Allmaras turbulence model is found most effective to capture a complex vortex structure. The adaptive mesh refinement method at a vortex center is also applied. Visualization of the computational results suggests that the second primary vortex may be a developing share layer merging to an open separation of the primary vortex. Not only the volume-mesh refinement but also the surface-mesh refinement is found important to capture Reynolds-number effects around a delta wing with a blunt leading edge.

## Introduction

DELTA wing has been used for space transport and supersonic transport because of high aerodynamic performance. Those transports utilize leading-edge separation at high angles of attack for take-off and landing. Analyses of the leading-edge separation have been performed by many experiments and computations. Previous numerical works about the leading-edge separation around a delta wing are given by for example, Ekaterinaris and Schiff,[1] and Murayama *et al.*[2]

Recent experiment at NASA Langley Research Center investigated effects of leading-edge bluntness and Reynolds-number difference.[3,4] In this experiment, the sharp and blunt leading edges are used. The sharp leading edge produces a typical conical vortex structure. Suction peak due to the leading-edge separation occurs almost at the same semispan locations for the entire wing. While the blunt leading edge produces a more complex flow. This leading edge delays the leading-edge separation onset downstream and another suction region appears inboard of the primary vortex. Reference 3 named this suction peak as the 'second primary vortex'.

Experiment also examined Reynolds-number effects quantitatively at the Reynolds numbers of 6 million and 60 million. In the case of the sharp leading edge, Reynolds-number effects are not significant because the separation point is fixed at the leading edge. Whereas, in the case of the blunt leading edge, the formation of the leading-edge vortex at the Reynolds number of 60 million is shifted downstream at least 20% root chord compared with that at the Reynolds number of 6 million.

In this paper, the second primary vortex has been investigated numerically through CFD visualization. Because of the high Reynolds number range in experiment, three turbulence models were examined. In addition, Reynolds-number effects were simulated and quantitative agreements were obtained.

## Computational Method

In this study, the unstructured mesh method[5,6] is used to simulate the flow field. The three-dimensional Navier-Stokes equations are computed with a finite-volume cell-vertex scheme. The unstructured hybrid mesh method[7] is applied to capture the boundary layer accurately and efficiently. The Harten-Lax-van Leer-Einfeldt-Wada Riemann solver[8] is used for the numerical flux computations. The Venkatakrishnan's limiter[9] is applied for reconstructing second order accuracy. The lower-upper symmetric-Gauss-Seidel implicit scheme[10] is applied for time integration.

Furthermore, in the unstructured hybrid mesh method, an adaptive mesh refinement method is used to increase the mesh resolution in the vicinity of the vortex centers.[11] Vortex centerlines are identified by the vortex-center identification method[12] as the distinct topological flow feature leading to the mesh refinement with accuracy and efficiency. In the region of tetrahedral unstructured mesh, a tetrahedra bisection algorithm is used.[13,14] The prisms are refined along the normal-to-surface direction to preserve the structure of the mesh in case hanging nodes are on the edges of the prisms.

*Graduate Student, Department of Aeronautics and Space Engineering. Student Member AIAA.
†Professor, Institute of Fluid Science. Associate Fellow AIAA.
‡Professor, Department of Aeronautics and Space Engineering. Associate Fellow AIAA.

## Turbulence Models

It is essential for accurate prediction of the leading-edge separation vortex at high Reynolds numbers not only to stifle the numerical diffusion but also to consider the influence of turbulence modeling. Therefore, the influence of turbulence models should be examined carefully.

In this study, the Goldberg-Ramakrishnan (G-R) one-equation model,[15] the Spalart-Allmaras (S-A) one-equation model[16] and the modified S-A one-equation model by Dacles-Mariani *et al.*[17] are compared without transition. In addition, the same cases are computed without any turbulence model for a comparison purpose (referred as a laminar flow later). The modified S-A model is briefly explained here:

1. The production term is modified to describe a scalar measure of the deformation tensor $S$ as the following equation using the strain rate $|s|$. Where, $\Omega_{ij}$ is the vorticity tensor, $S_{ij}$ is the strain velocity tensor.

$$S = |\omega| + 2\min(0., |s| - |\omega|) \tag{1a}$$

$$|\omega| = \sqrt{2\Omega_{ij}\Omega_{ij}} = \sqrt{\frac{1}{2}\left(\frac{\partial U_i}{\partial x_j} - \frac{\partial U_j}{\partial x_i}\right)^2} \tag{1b}$$

$$|s| = \sqrt{2S_{ij}S_{ij}} = \sqrt{\frac{1}{2}\left(\frac{\partial U_i}{\partial x_j} + \frac{\partial U_j}{\partial x_i}\right)^2} \tag{1c}$$

The production term of the original S-A model depends only on the vorticity $|\omega|$. However, because the value of the production term becomes large in vortical flows, the resulting turbulent kinematic viscosity becomes too large. This acts as the numerical diffusion to a vortex. The strain rate is introduced to overcome this overestimation, so that the production term is limited. This method using both the vorticity tensor and the strain velocity tensor is suggested by Kato-Launder in the improved $k$-$\epsilon$ two-equation turbulence model.[18]

2. In the original S-A model, the destruction term disappears completely in the far-wall region. A modification to this term is implemented by checking the ratio between production and dissipation of the standard high Reynolds number Jones-Launder $k$-$\epsilon$ model[19] using the term $P_k$.

$$dest = \max\left(\rho c_{w1} f_w \left(\frac{\widetilde{\nu}}{d}\right)^2, \frac{c_\mu}{c_1 c_2 c_{b1}}\rho\widetilde{\nu} \cdot \frac{1}{2}\sqrt{P_k}\right) \tag{2a}$$

$$P_k = \frac{\partial U_i}{\partial x_j}\left(\frac{\partial U_i}{\partial x_j} + \frac{\partial U_j}{\partial x_i} - \frac{2}{3}\delta_{ij}\frac{\partial U_k}{\partial x_k}\right) \tag{2b}$$

where the constant values of $c_\mu$, $c_1$ and $c_2$ are taken from the original Jones-Launder $k$-$\epsilon$ model. The constant value of $c_{b1}$ is taken from the original S-A model.

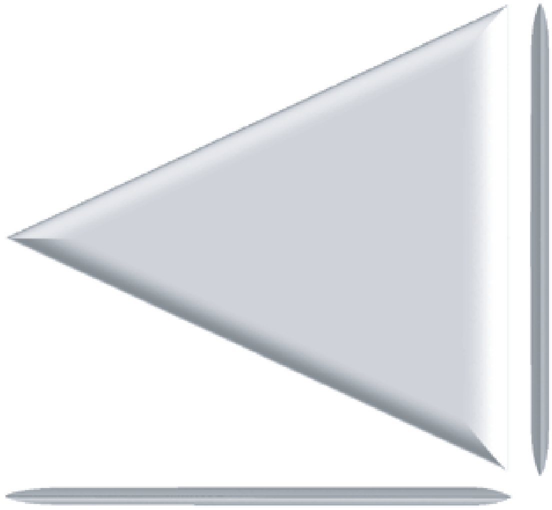

**a) Three views of computational geometry**

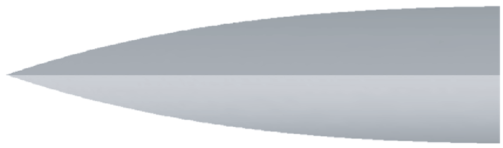

**b) Close-up view of sharp leading edge**

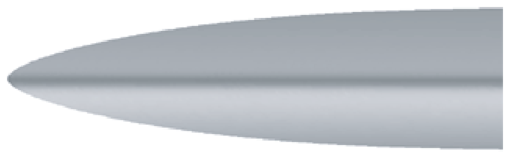

**c) Close-up view of blunt leading edge**

**Fig. 1 Delta wing geometries for numerical simulation.**

Reference 20 reported that this modified S-A model captured the wing tip vortex successfully.

## Results

The geometries used in the present study are based on the wind tunnel models in Ref. 3. They correspond to sharp and blunt leading edge shapes at a sweep angle of 65 deg. The present research focuses on the blunt leading edge named as 'medium-radius leading edge' in Ref. 3. Figure 1 shows the delta wing geometries with the sharp and the blunt leading edge for numerical simulation. The flow conditions are a Mach number of 0.4, an angle of attack of 13 deg and the Reynolds numbers of 6 million and 60 million based on the wing mean aerodynamic chord.

### Bluntness Effect

The bluntness effect is discussed with flows around sharp and blunt leading edges at the Reynolds number of 6 million. The unstructured hybrid mesh is generated, and then the adaptive mesh refinement method is applied to improve the mesh resolution in the vicinity of the vortex center. Figures 2a and 2b show the vortex

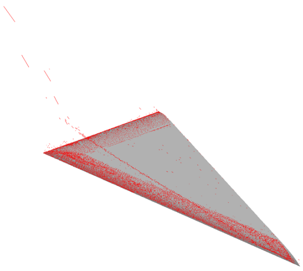

a) Vortex centerlines used as refinement indicator

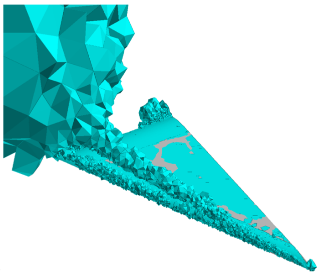

b) Cells containinig vortex centerlines and neighbouring cells

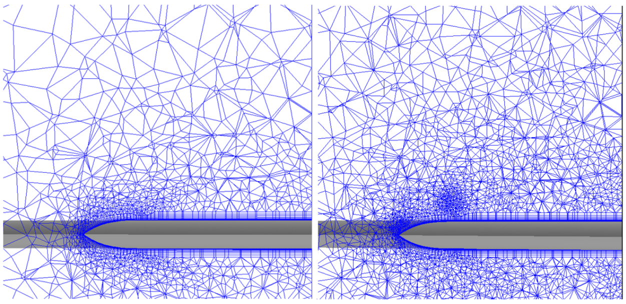

c) Crossflow plane at 60% root chord; initial mesh (left) and adaptive mesh (right)

**Fig. 2 Adaptive refinement for the sharp leading-edge case.**

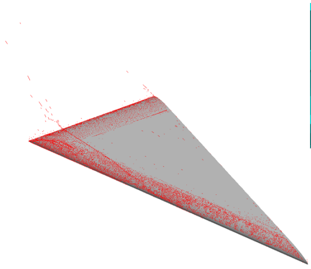

a) Vortex centerlines used as refinement indicator

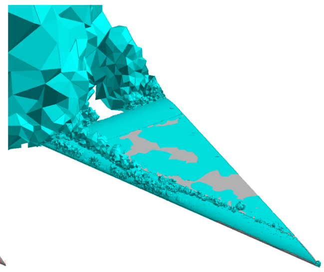

b) Cells containinig vortex centerlines and neighbouring cells

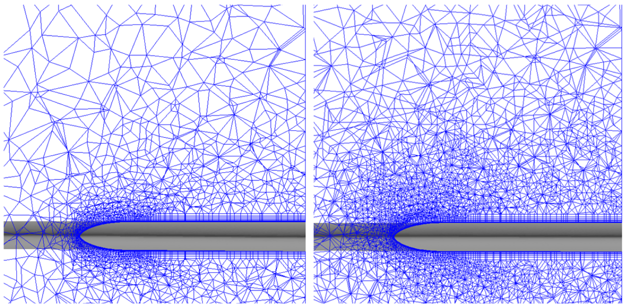

c) Crossflow plane at 60% root chord; initial mesh (left) and adaptive mesh (right)

**Fig. 3 Adaptive refinement for the blunt leading-edge case.**

centerlines and their neighbouring cells, respectively, for the sharp leading-edge case. Figure 2c shows crossflow plane views of the initial and the refined meshes at 60% location of the root chord. Figure 3 shows similar views for the blunt leading-edge case. The comparison of all mesh numbers are summarized in Fig. 4. Large increase of number of tetrahedra indicates that the mesh resolution is mainly improved at the vicinity of the vortex center.

*Adaptive Refinement and Turbulence Model Effects in the Sharp Leading-Edge Case*

Computed surface pressure distributions are compared at 40 and 60% locations of the root chord with experiment in Figs. 5 and 6, respectively. From Figs. 5a and 6a, the adaptive refinement is found to improve the suction peak of the primary vortex. Although the position of the suction peak is predicted correctly, the value of the suction peak does not agree well with experiment. In Fig. 6, the computed pressure distribution at the inboard wing does not agree well with experiment, either, because no sting fairing is modeled in this computation.

To improve the numerical prediction of the suction peak, the original and modified S-A turbulence models are applied in addition to the laminar flow computation as shown in Figs. 5b and 6b. In the case of the laminar flow simulation, the suction peak appears worst among the computations. The original S-A model performs similar to the G-R model. In Fig. 5b, the modified S-A model is found to predict the suction peak much better than others. In Fig. 6b, the modified S-A turbulence model also captures the suction peak of the secondary vortex. The corresponding surface streamlines in Fig. 7 shows the secondary separation as well as the tertiary separation. Further improvements might require higher order space discretization, for example, the compact scheme.

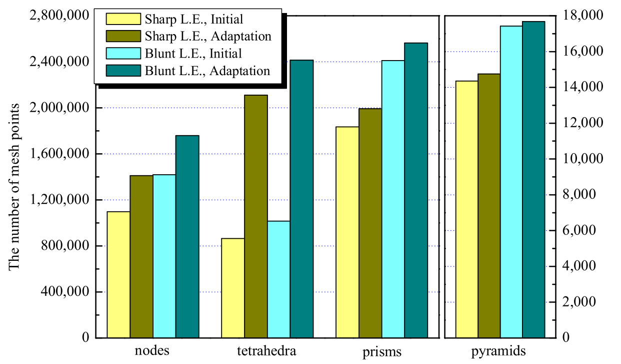


**Fig. 4 Comparison of volume meshes for sharp and blunt leading-edge cases.**

The modified S-A model improves the production and destruction terms of the turbulence transport equation of the original S-A model. These two terms are examined, respectively, to identify the key influence to capture the secondary separation. Figure 8

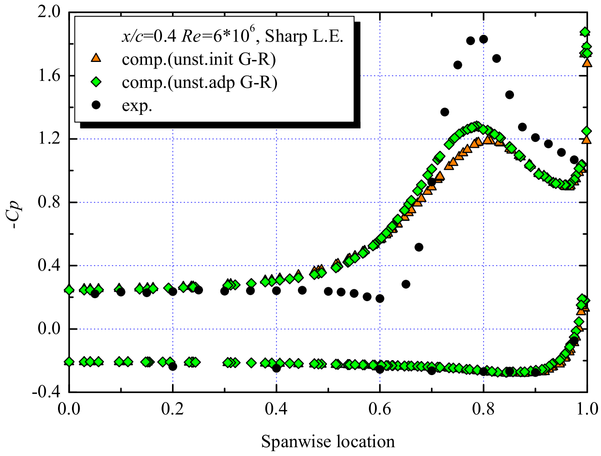


a) **Effect of adaptive mesh refinement**

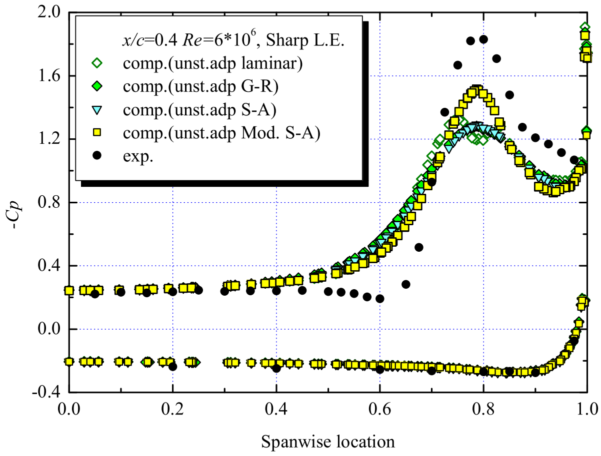


b) **Effect of turbulence modeling**

**Fig. 5 Comparison of computed surface pressure coefficients with experiment for a flow past the sharp leading edge at $x/c = 0.4$.**

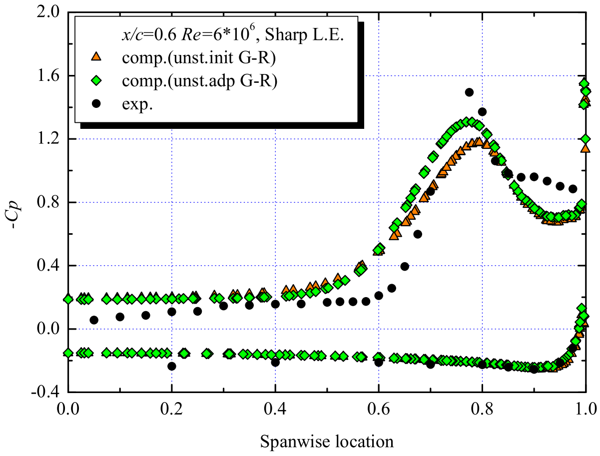


a) **Effect of adaptive mesh refinement**

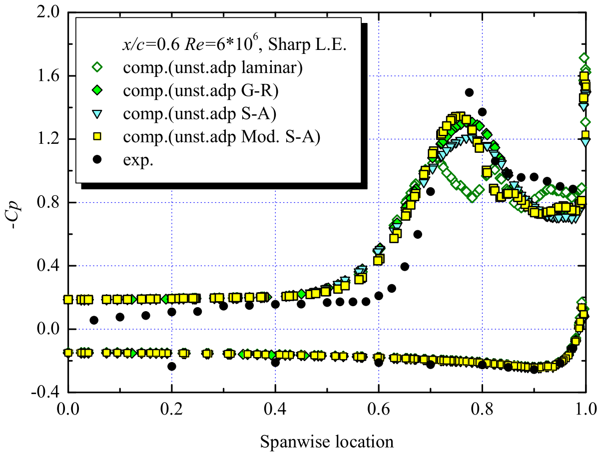


b) **Effect of turbulence modeling**

**Fig. 6 Comparison of computed surface pressure coefficients with experiment for a flow past the sharp leading edge at $x/c = 0.6$.**

reveals that the production term has the influence while the destruction term does not.

According to the modification in Eq. (1a) for the production term of the transport equation, the value of the eddy viscosity becomes smaller in the vortical region. Figure 9 shows comparisons of contours at a crossflow plane and isosurfaces of the computed eddy viscosities between the original and the modified S-A models. It reveals that the modified S-A model captures the detailed vortex structure and restrains amount of eddy viscosity.

### *The Second Primary Vortex in the Blunt Leading-Edge Case*

The experiment suggests that blunt leading edge delays primary separation downstream and that another suction region, named as the second primary vortex, appears inboard of the primary vortex from 40% to 60% location of the root chord. The computed surface pressure distributions at 20, 40 and 60% locations of the root chord in the blunt leading-edge case are compared with experiment in Fig. 10. Figure 10a shows that the laminar computation forms the primary vortex too early. This suggests the necessity of a turbulence model because the turbulence models predict the attached flow near the wing apex. The modified S-A model predicts the secondary vor-

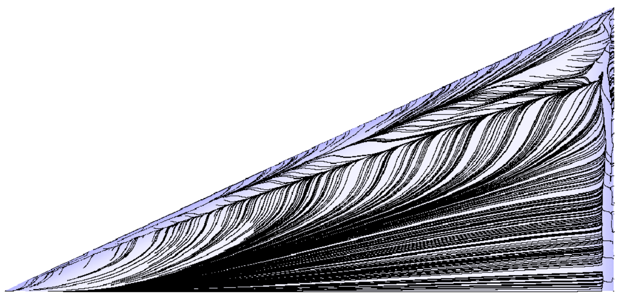

**Fig. 7 Computed surface streamlines for a flow past the sharp leading edge using the modified S-A model at the Reynolds number of 6 million.**

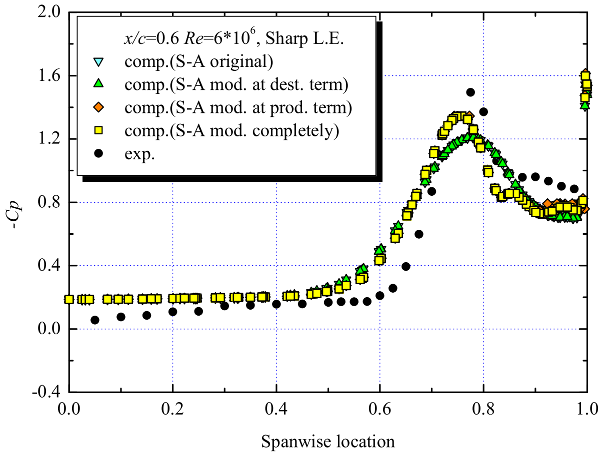


**Fig. 8 Comparison of surface pressure coefficients with experiment by using various S-A model modifications.**

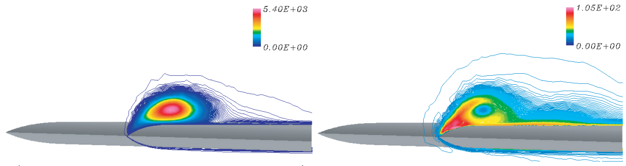

**a) Crossflow plane at $x/c = 0.6$**

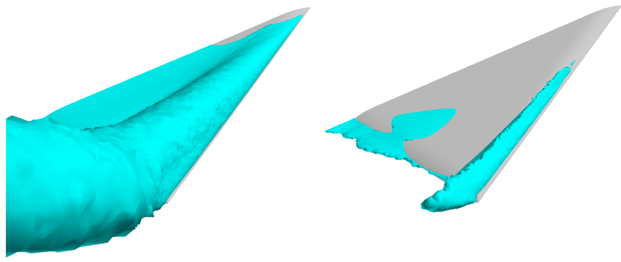

**b) Isosurface of value=80**

**Fig. 9 Visualization of eddy viscosity for a flow past the sharp leading edge; using the S-A model (left) and using the modified S-A model (right).**

tex similar to the sharp leading-edge case. Especially only this model shows a relatively flat pressure distribution at the 40% chord station from the 70% to 90% semispan region in Fig. 10b, indicating the formation of the second primary vortex. Moreover, this turbulence model successfully predicts that the separation suction peak moves downstream due to bluntness. Figure 11 shows that the modified S-A model captures a vortex structure better than the original S-A model.

Figure 12 shows the computed surface streamlines and pressure distribution using the modified S-A model. The region of pressure plateau shown in Fig. 10b is found at 35–57% root chord. Its location agrees well with experiment. Figure 13 shows the vortex structure using helicity contours at the crossflow plane. It is found that the first primary and the second primary vortices rotate in the same direction. Figure 14 shows the comparison of the streamlines between near the wall and through the second primary vortex. This figure indicates streamlines near the wall at the wing apex flow straight to downstream, while streamlines inside of the boundary layer merge into the second primary vortex. Figure 15 reveals that the share layer occurs from the leading edge. Figure 16 shows the separation lines on the upper surface of the wing. Separation occurs in the middle of the blunt leading edge. This separation line suggests Open Separation.[21,22] The second primary vortex suggested in experiment is found to be a developing share layer merging to the open separation. This shear layer is perhaps common in the open separation, but it happens to be emphasized due to the combination of the geometry and flow condition in this case. In the case of the sharp leading edge, the separation is a closed separation because a separation line always starts from a wing apex. Then, the flow has a typical, conical structure.

### Reynolds-Number Effects

The computational conditions at the Reynolds numbers of 6 million and 60 million are chosen to examine Reynolds-number effects. The delta wing only with the blunt leading edge is computed because Reynolds-number effects are found pronounced in the blunt leading-edge case. The mesh with 95,624 surface mesh points is used for both Reynolds numbers, and the refined mesh with 169,458 surface mesh points is used for the Reynolds number of 60 million. The close-up views of both surface meshes in the vicinity of the wing tip are shown in Fig. 17. Comparison of the meshes is summarized in Fig. 18. Although the number of tetrahedron points is not so large in the case of fine surface mesh because of no adaptive mesh refinement, the fine mesh has larger prisms in proportion to the increased surface mesh points near the wall. The coarse and fine meshes have maximum dimensionless wall distances $y^+_{\max}$ of 4.06 and 1.46, respectively, at the first mesh points from the wall.

The computed surface pressure distributions at 40, 60 and 80% locations of the root chord using the G-R and the modified S-A model are compared with experiment in Figs. 19 and 20, respectively. The G-R model predicts too large separation on the coarse mesh even with the adaptation and too small separation on the fine mesh. The original S-A model is similar to the G-R model and thus the result is not shown here. Only the fine-mesh result using the modified S-A model predicts the separation onset similar to experiment. The suction peak, however, is not captured adequately in Fig. 20c because the mesh is not fine enough. The adaptive mesh refinement was not applied to the fine mesh because the memory requirement became too large. These figures reveal a fine surface mesh is needed at least to capture the separation onset correctly at the high Reynolds number. Figure 21 shows the comparison of surface streamlines using the G-R and modified S-A models. This figure shows that the modified S-A model captures the separation and attachment lines of the primary and secondary vortices.

The leading-edge pressure distributions are shown in Fig. 22 to indicate a separation onset. Computational results about the separation onset agree with experimental trend. Figure 23 shows the comparison of computed vortex centerlines at both Reynolds numbers using the G-R and the modified S-A models. This figure shows that the G-R model predicts the separation onset downstream compared with experiment, whereas that the separation onset using the modified S-A model agrees well with experiment. The modified S-A model predicted Reynolds-number effects quantitatively.

## Conclusion

Numerical simulation around delta wings with sharp and blunt leading edges has been performed on unstructured hybrid mesh to investigate the leading-edge bluntness and Reynolds-number effects suggested by experiment. The modified Spalart-Allmaras one-equation turbulence model was found most accurate to capture the complex vortex structure including the secondary vortex. At the Reynolds number of 6 million, this model captured the second primary successfully as indicated in experiment. The visualizations of the computational results suggested that this second primary vortex is a developing share layer merging to the open separation due to the leading-edge bluntness.

The computation at the Reynolds number of 60 million using the modified S-A model predicts the Reynolds-number effect of delayed onset of the leading-edge separation successfully. Not only the volume-mesh refinement but also surface-mesh refinement was found important to capture Reynolds-number effects.

## Acknowledgement

The present computation was carried out using the supercomputer, SX-5, in Institute of Fluid Science, Tohoku University.

## References

[1]Ekaterinaris, J. A. and Schiff, L. B., "Numerical Prediction of Vortical Flow over Slender Delta Wings," *Journal of Aircraft*, Vol. 30, No. 6, 1993, pp. 935–942.

[2]Murayama, M., Nakahashi, K., Obayashi, S., and Kato, T., "Numerical Simulation of Vortical Flows Using Vorticity Confinement Coupled with Unstructured Adaptive Grid Refinement," *Computational Fluid Dynamics Journal*, Vol. 10, No. 1, 2001, pp. 28–36.

[3]Luckring, J. M., "Reynolds Number and Leading-Edge Bluntness Effects on a 65° Delta Wing," AIAA Paper 2002-0419, 2002.

[4]Chu, J. and Luckring, J. M., "Experimental Surface Pressure Data Obtained on 65° Delta Wing Across Reynolds Number and Mach Number Ranges," NASA TM-4645, Feb. 1996.

[5]Ito, Y. and Nakahashi, K., "Surface Triangulation for Polygonal Models Based on CAD Data," *International Journal for Numerical Methods in Fluids*, Vol. 39, Issue 1, 2002, pp. 75–96.

[6]Sharov, D. and Nakahashi, K., "Hybrid Prismatic/Tetrahedral Grid Generation for Viscous Flow Applications," AIAA Paper 96-2000, 1996.

[7]Ito, Y. and Nakahashi, K., "Unstructured Mesh Generation for Viscous Flow Computations," *Proceedings of the 11$^{th}$ International Meshing Roundtable*, Ithaca, NY, 2002, pp. 367–377.

[8]Obayashi, S. and Guruswamy, G. P., "Convergence Acceleration of an Aeroelastic Navier-Stokes Solver," *AIAA Journal*, Vol. 33, No. 6, 1994, pp. 1134–1141.

[9]Venkatakrishnan, V., "On the Accuracy of Limiters and Convergence to Steady State Solutions," AIAA Paper 93-0880, 1993.

[10]Sharov, D. and Nakahashi, K., "Reordering of Hybrid Unstructured Grids for Lower-Upper Symmetric Gauss-Seidel Computations," *AIAA Journal*, Vol. 36, No. 3, 1998, pp. 484–486.

[11]Murayama, M., Nakahashi, K., and Sawada, K., "Simulation of Vortex Breakdown Using Adaptive Grid Refinement with Vortex-Center Identification," *AIAA Journal*, Vol. 39, No. 7, July 2001, pp. 1305–1312.

[12]Sawada, K., "A Convenient Visualization Method for Identifying Vortex Centers," *Transactions of the Japan Society for Aeronautical and Space Sciences*, Vol. 38, No. 120, 1995, pp. 102–116.

[13]Rivara, M. C., "Selective Refinement/Derefinement Algorithms for Sequences of Nested Triangulations," *International Journal of Numerical Methods in Engineering*, Vol. 28, No. 6, 1989, pp. 2889–2906.

[14]Sharov, D. and Fujii, K., "Three-Dimensional Adaptive Bisection of Unstructured Grids for Transient Compressible Flow Computations," AIAA Paper 95-1708, 1995.

[15]Goldberg, U. C. and Ramakrishnan, S. V., "A Pointwise Version of the Baldwin-Barth Turbulence Model," *Computational Fluid Dynamics*, Vol. 1, 1993, pp. 321–338.

[16]Spalart, P. R. and Allmaras, S. R., "A One-Equation Turbulence Model for Aerodynamic Flows," AIAA Paper 92-0439, 1992.

[17]Dacles-Mariani, J., Zilliac, G. G., Chow, J. S., and Bradshaw, P., "Numerical/Experimental Study of a Wingtip Vortex in the Near Field," *AIAA Journal*, Vol. 33, No. 9, 1995, pp. 1561–1568.

[18]Kato, M. and Launder, B. E., "The Modelling of Turbulent Flow around Stationary, and Vibrating Square Cylinder," *Proceedings of 9$^{th}$ Symposium of Turbulent Shear Flows*, Paper 10-4-1, 10-4-6, 1993.

[19]Jones, W. P. and Launder, B. E., "The Prediction of Laminarization with a Two Equation Model of Turbulence," *International Journal of Heat and Mass Transfer*, Vol. 15, 1972, pp. 301–314.

[20]Fares, E., Meinke, M., and Schöder, W., "Numerical Simulation of the Interaction of Wingtip Vortices and Engine Jets in the Near Field," AIAA Paper 2000-2222, 2000.

[21]Wang, K. C., "Separation Patterns of Boundary Layer over on Inclined Body of Revolution," *AIAA Journal*, Vol. 10, No. 8, 1972, pp. 1044–1050.

[22]Wang, K. C., "Boundary Layer over a Blunt Body at High Incidence with an Open-Type Separation," *Proceedings of Royal Society, London*, A. 340, 1974, pp. 33–55.

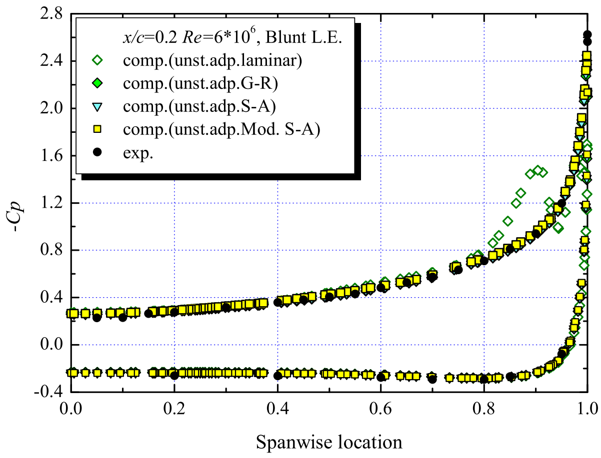


a) $x/c = 0.2$

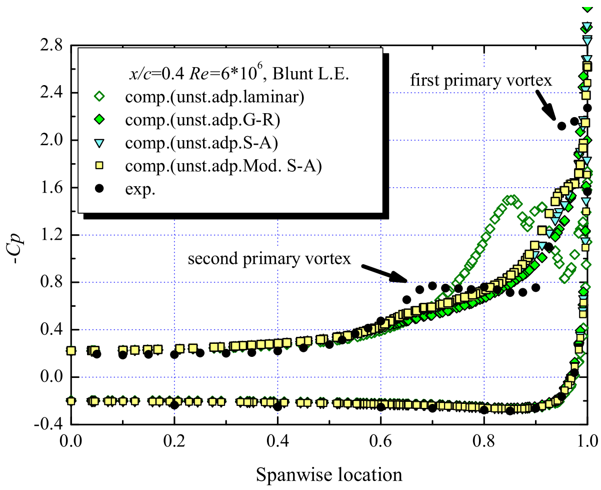


b) $x/c = 0.4$

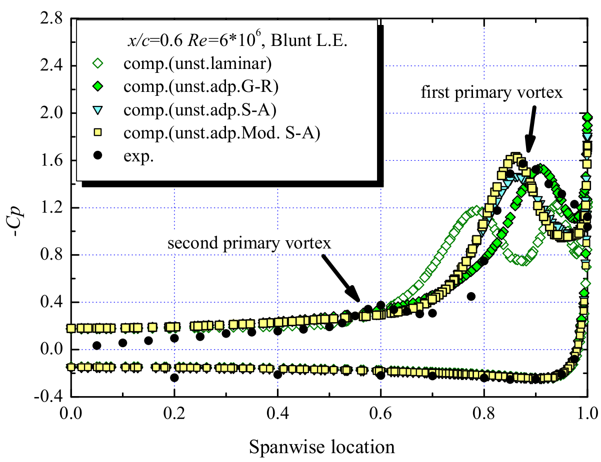


c) $x/c = 0.6$

**Fig. 10** Comparison of computed surface pressure coefficients with experiment for a flow past the blunt leading edge at the Reynolds number of 6 million.

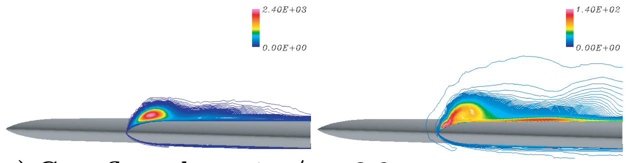

a) Crossflow plane at $x/c = 0.6$

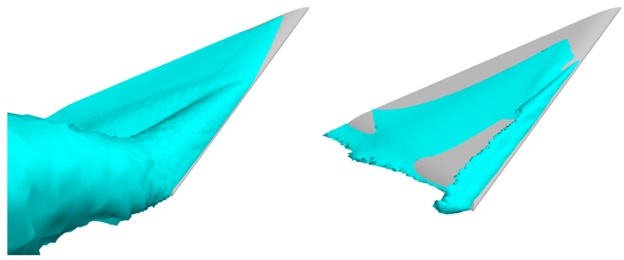

b) Isosurface of value=80

**Fig. 11** Visualization of eddy viscosity for a flow past the blunt leading edge; using the S-A model (left) and using the modified S-A model (right).

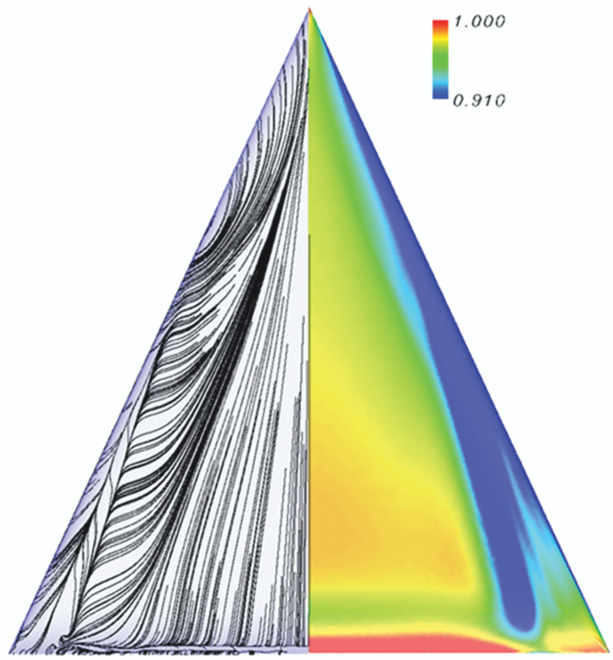


**Fig. 12** Computed surface streamlines (left) and pressure distribution (right) for a flow past the blunt leading edge using the modified S-A model at the Reynolds number of 6 million.

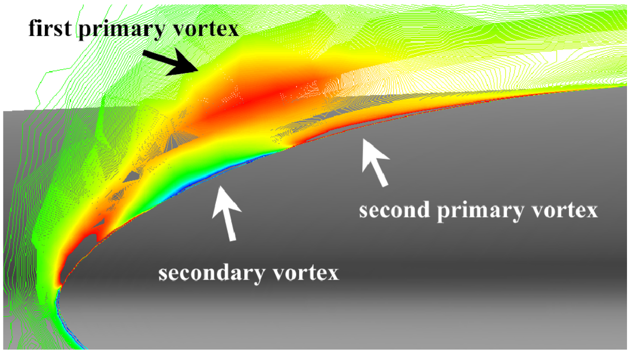


**Fig. 13** Computed helicity contours crossflow plane at 40% for a flow past the blunt leading edge using the modified S-A model.

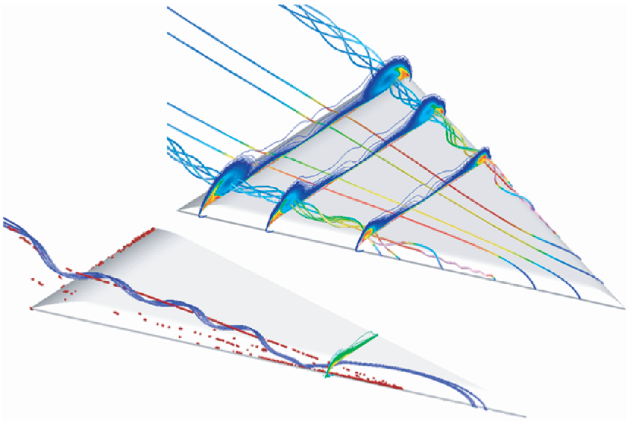

**Fig. 14** Comparison of computed streamlines; starting from outside of the boundary layer (top), starting from inside of the boundary layer and going through the second primary vortex (bottom).

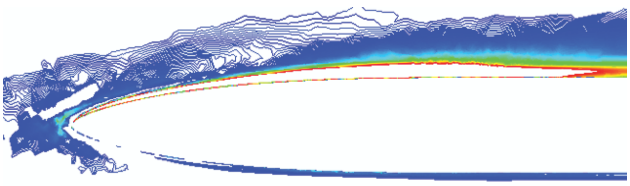

**Fig. 15** Computed helicity contours using the modified S-A model on chordwise view at 24% location where a second primary vortex exists.

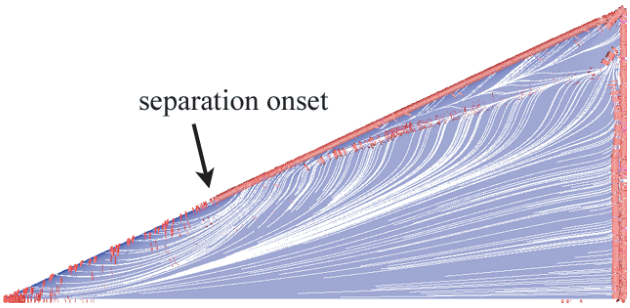


**Fig. 16** Computed separation lines and surface streamlines.

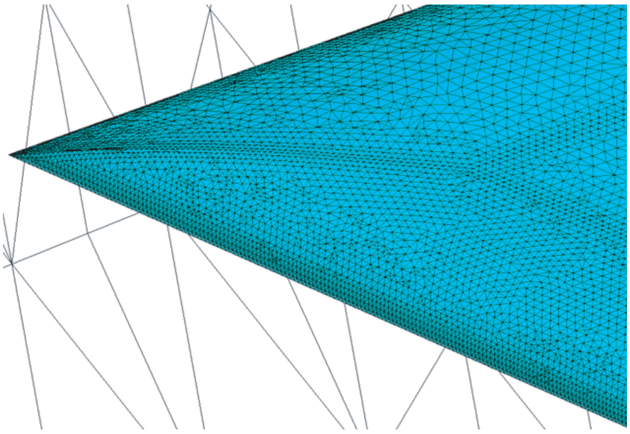

a) Close-up view of coarse mesh with adaptive refinement

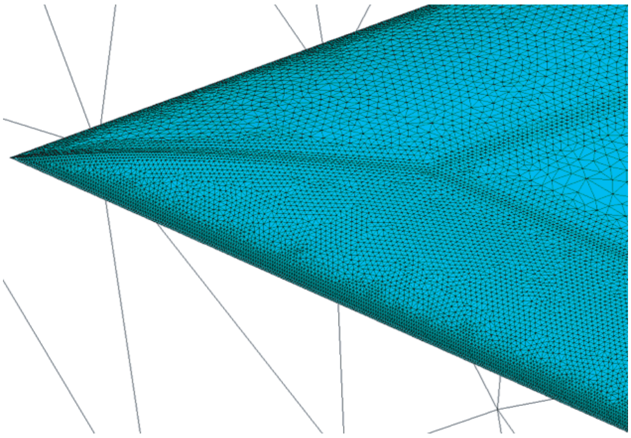

b) Close-up view of fine mesh

**Fig. 17** Comparison of unstructured mesh at wing tip area.

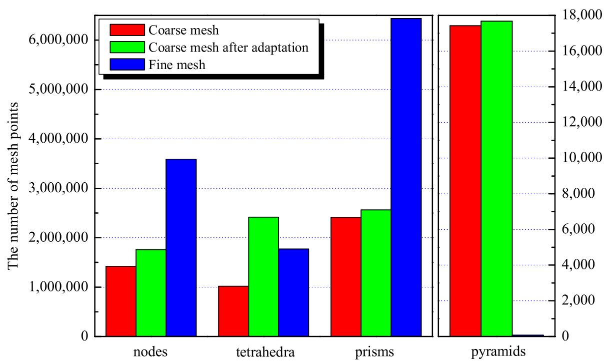


**Fig. 18** Comparison of volume meshes between coarse and fine meshes.

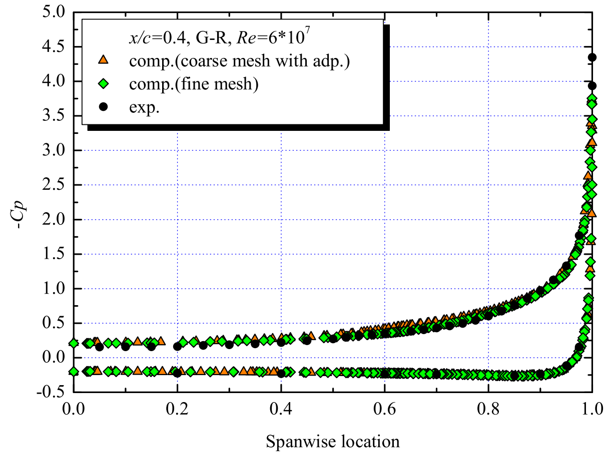


a) $x/c = 0.4$

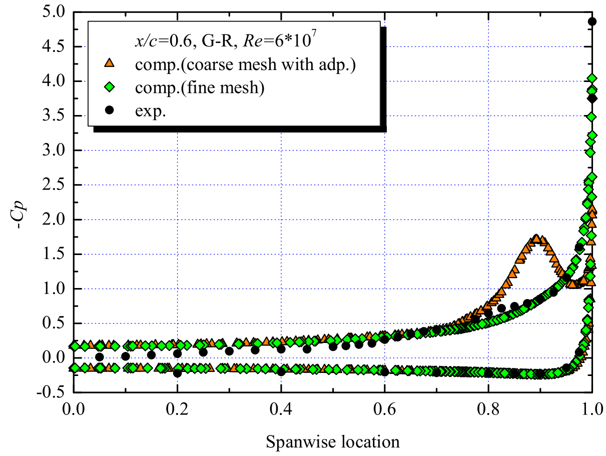


b) $x/c = 0.6$

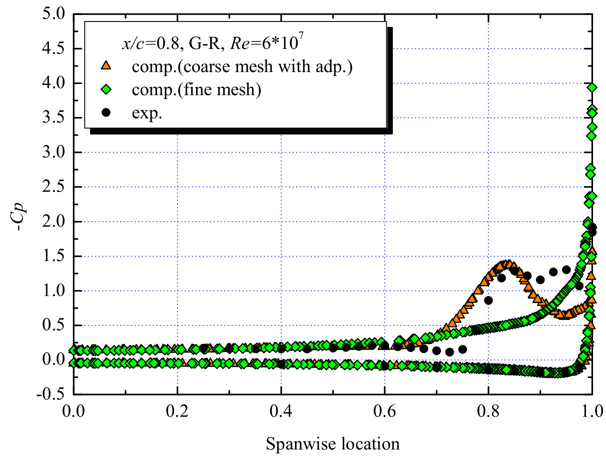


c) $x/c = 0.8$

**Fig. 19 Comparison of computed surface pressure distributions with experiment using the G-R turbulence model at the Reynolds number of 60 million.**

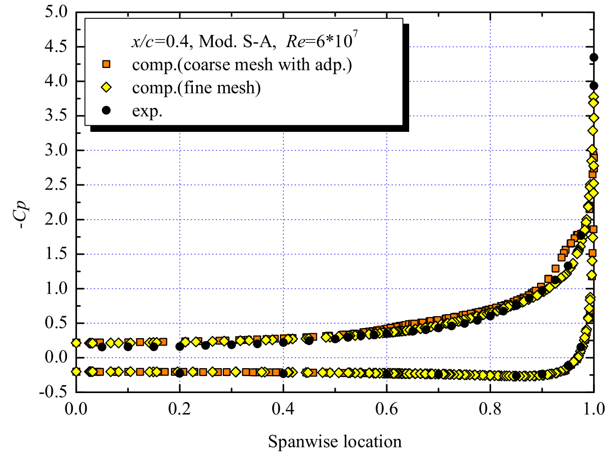


a) $x/c = 0.4$

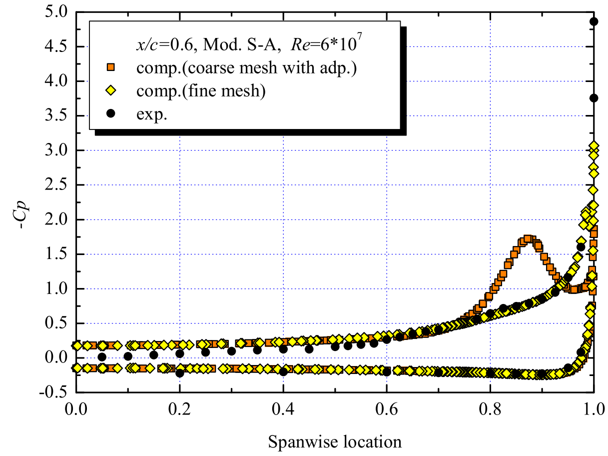


b) $x/c = 0.6$

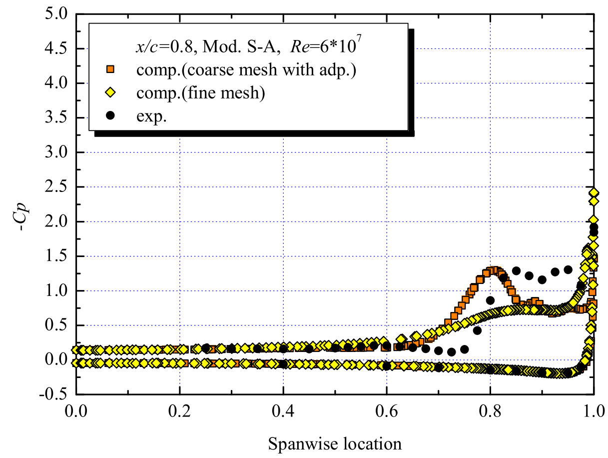


c) $x/c = 0.8$

**Fig. 20 Comparison of computed surface pressure distributions with experiment using the modified S-A turbulence model at the Reynolds number of 60 million.**

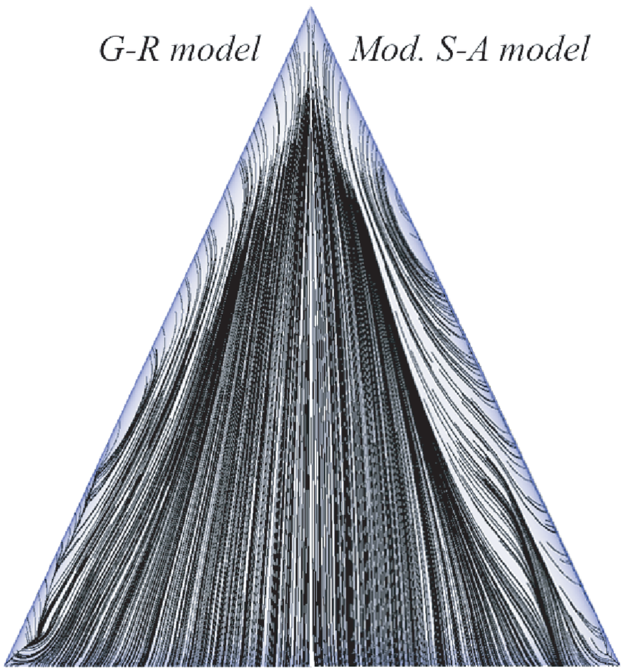


**Fig. 21** Computed surface streamlines at the Reynolds number of 60 million using the G-R model (left) and the modified S-A model (right) on the fine mesh.

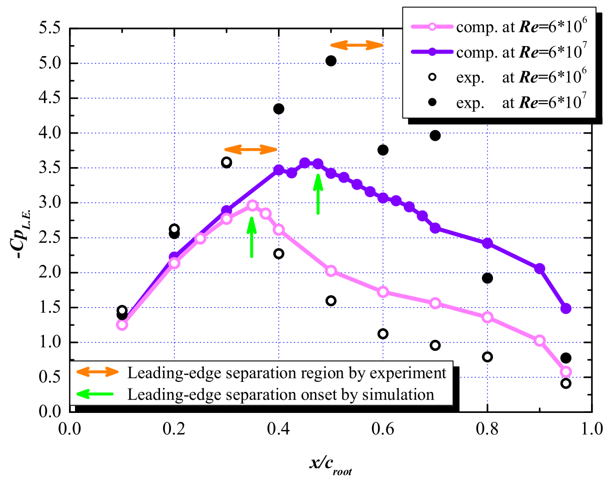


**Fig. 22** Comparison of leading-edge pressure distributions using the modified S-A model at the Reynolds numbers of 6 million and 60 million with experiment.

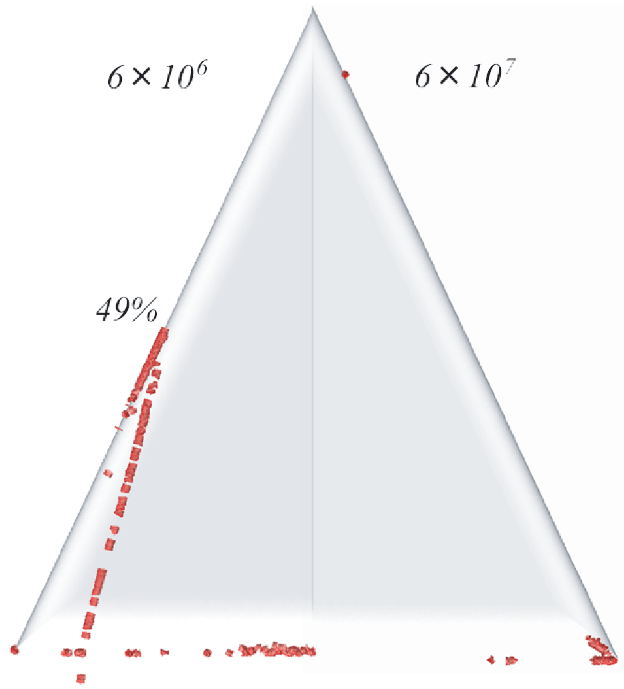


a) Vortex centerlines using the G-R turbulence model

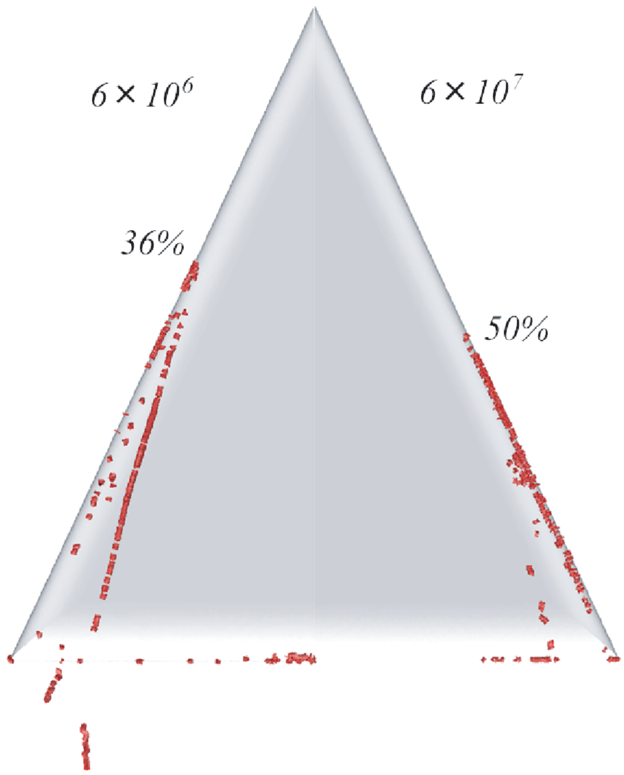


b) Vortex centerlines using the modified S-A turbulence model

**Fig. 23** Comparison of computed vortex centerlines and separation onset points at the Reynolds number of 6 million (left) and 60 million (right).